Advanced Optical Materials

ADVANCED OPTICAL MATERIALS
www.advopticalmat.de

RESEARCH ARTICLE OPEN ACCESS

Digital Twin of a One-Sun-Driven Luminescent-Concentrator-Assisted Planar Solar-Pumped Fiber Laser

Anvarjon Sherniyozov[1] | Dmitry Busko[1] | Bryce S. Richards[1,2]

[1]Institute of Microstructure Technology, Karlsruhe Institute of Technology, Eggenstein-Leopoldshafen, Germany | [2]Light Technology Institute, Karlsruhe Institute of Technology, Karlsruhe, Germany

Correspondence: Bryce S. Richards (bryce.richards@kit.edu)

Received: 12 May 2026 | **Revised:** 19 June 2026 | **Accepted:** 3 July 2026

Keywords: luminescent solar concentrators (LSC) | Monte Carlo simulation | optical confinement | photon–core coupling | rate equation modeling | solar-pumped fiber lasers

ABSTRACT

Planar solar-pumped fiber lasers (SPFLs) based on luminescent solar concentrators (LSCs) enable direct conversion of one-sun irradiation into laser radiation. However, experimentally demonstrated performance remains limited, while the underlying mechanisms are insufficiently understood. In this work, a physics-based digital twin of LSC-assisted SPFL is developed using Monte Carlo ray tracing with explicit fiber geometry, coupled to rate-equation and power-propagation modeling. The model is validated against differential-gain and laser-output measurements. The analysis reveals that SPFL performance is constrained by weak photon–core interaction arising from the µm-scale core and low single-pass absorption probability in the Nd^{3+}-doped core. In the experimentally validated configuration, only 0.54% (0.34 W) of the incident power is absorbed within the core, corresponding to 35 mW laser output. Photon-flux analysis identifies 51.2% material-related losses and 48.3% cavity-related confinement losses associated with angular-dependent dichroic-mirror performance. Parameter studies demonstrate sensitivity of SPFL performance to sensitizer photoluminescence quantum yield, LSC refractive-index distribution, sensitizer thickness, and core diameter. Combining several improvement strategies within the present architecture yielded approximately 470 mW laser output and 0.67% solar-to-laser conversion efficiency representing 13-fold improvement relative to the baseline system (0.05%). The developed digital twin enables systematic investigation of alternative architectures and optimization of one-sun SPFLs.

1 | Introduction

The efficient conversion of solar radiation into application-ready energy forms remains a central goal in renewable energy research, driven by the increasing global energy demand and the environmental consequences of fossil fuel use, contrasted against the abundance, sustainable nature, and low-cost potential of solar energy. While sunlight is often converted into electricity or thermal energy, there is also the possibility of generating optical power. Within the latter category, directly solar-pumped lasers (SPL) offer a distinctive route by converting solar radiation directly into a coherent laser beam. Their unique characteristics coherence, spectral precision, and directionality enable efficient energy utilization across diverse applications [1, 2].

The concept of the SPL was first proposed in 1962 [3], with early experimental demonstrations utilizing CaF_2:Dy^{2+} [4] and Nd^{3+}-doped yttrium aluminum garnet (YAG)laser rod in 1966 [5], which achieved continuous-wave laser output of 1 W. Over the following decades, the focus shifted from demonstrating laser operation to improving solar-to-laser conversion efficiency. Significant progress was achieved, exemplified by Liang et al., who demonstrated state-of-the-art solar-pumped solid-state lasers operating under highly concentrated sunlight (on the order of 10^3 suns), yielding 16.5 W of continuous-wave multimode output from 356 W of incident solar power, corresponding to a solar-to-laser efficiency of 4.64% [6].

To contextualize this performance, direct solar-to-laser conversion can be compared with a cascaded process, in which photovoltaic cells generate electricity to drive a diode-pumped laser. A simple estimate, assuming a solar cell efficiency of 20%–25% and a diode-pumped laser wall-plug efficiency of approximately 20%, yields an overall solar-to-laser efficiency on the order of 4%–5%. Notably, this range is comparable to the highest efficiencies reported for direct SPL systems [6]. Further improvements in SPL performance may be achieved through enhanced spectral utilization [7], for example by incorporating sensitizers that transfer energy to the active lasing ions via radiative and nonradiative pathways, and by optimizing laser configurations to improve solar-to-medium optical coupling. Although such projections remain speculative, solar-to-laser efficiencies approaching double-digit values have been proposed as a target [8], and would represent a significant milestone, corresponding to a substantial increase beyond the effective limits of current cascaded conversion schemes. By eliminating intermediate conversion stages, SPL systems avoid multistage complexity and cumulative losses, offering a simpler pathway for solar energy utilization.

Several studies have emerged in which, instead of solid-state gain media, optical fibers are employed as the lasing medium for solar powered lasers. Simulation-based studies predicted solar-to-laser efficiencies of 2%–2.5% using off-axis parabolic mirror array pumping configurations [9] and by employing multicore fibers [10]. Similar to solid-state-based SPLs, which typically rely on primary and secondary concentrators and require solar tracking [11], these works [9, 10] also utilized concentrated illumination in their models. More recently, conceptually simpler planar solar-pumped fiber lasers (SPFLs) have been proposed [12], which can operate without geometrical focusing optics and thus do not require solar tracking. While this approach offers architectural simplicity, SPFLs are in an early developmental stage, and experimentally demonstrated efficiencies remain low compared to concentrator-based systems. This work focuses on planar solar-pumped fiber lasers (SPFLs), given their conceptually elegant design and potential for operating under non-concentrated sunlight—so-called “one sun” operation.

The use of a fiber-based configuration as an alternative to classical laser rods (e.g., Nd^{3+}-YAG) appears to have been first suggested around 2012 [13], motivated by the idea that eliminating focusing optics could enable a simpler and less-bulky lasing system to be realized. That work reported positive gain in an Nd^{3+}-doped active fiber pumped by a low-concentration, xenon lamp-based solar simulator. A subsequent experimental realization [14] of a low-concentration, directly SPFL was demonstrated using a 40 m-long Nd^{3+}-doped fiber coil enclosed within a ring-shaped chamber filled with a sensitizer solution, comprised of a fluorescent organic dye dissolved in a solvent. The system achieved lasing at a threshold corresponding to approximately 15 suns. This represents the first attempts to pump a SPFL using spectral concentration—i.e., using luminescent materials to selectively absorb light in unutilized regions of the solar spectrum and then re-emit this at wavelengths that can be absorbed by the Nd^{3+}-fiber—rather than simply geometrically concentrating all wavelengths using lenses or mirrors.

Later in 2019, two related studies were conducted to investigate the factors limiting the performance of SPFL. In the first work, Bisson et al. [15] examined the effect of the thermally-excited lower laser level in Nd^{3+}-doped fibers and concluded that the small, thermally-excited population in the $^4I_{11/2}$ Stark level is primarily responsible for absorption losses at the laser wavelength at room temperature. In the second study, Endo et al. [16] proposed a design concept for a transversely-excited SPFL and developed a Monte Carlo model to predict its performance.

A series of studies in a Japanese-German collaboration progressed the development of planar, directly SPFL based on the concept of a luminescent solar concentrator (LSC). The LSC is essentially a luminescent waveguide, whereby the fluorescence emitted by organic dyes is trapped within the sheet via total internal reflection, thus achieving spectral concentration of light around the edges of the disc, where the fibers are located. In contrast to the aforementioned work, the LSC achieves spectral concentration within a solid-state device, much easier to handle than the older liquid-filled sensitizer units. While spectral concentration has previously been used in other optical technologies—e.g., for enhancing the performance of non-linear up-conversion systems [17]—it has not been applied to pumping SPFLs before.

In 2020, the first demonstration of lasing in a fully-planar SPFL without any focusing optics was reported, employing a LSC combined with a fiber laser of transverse-excitation geometry under natural sunlight [12]. The 30 cm-diameter device achieved a maximum output power of 1.3 mW centered at 1090 nm. In the same year, the sensitizing potential of all-inorganic cesium lead halide perovskite nanocrystals was examined for SPFL applications [18]. Using the experimental setup established in earlier work [14], the perovskite-based system performed worse than the previously used Rhodamine 6G dye-sensitized case. This decrease in performance was attributed to a 10 nm spectral misalignment between sensitizer photoluminescence (PL) peak and Nd^{3+} ion absorption peak at 580 nm (transition from $^4I_{9/2}$ ground state to the $^4G_{5/2}$ / $^2G_{7/2}$ excited states). Numerical analysis indicated that optimized nanocrystals could serve as promising sensitizers for future implementations. This example of a 10 nm spectral misalignment serves to highlight the sensitivity of SPFL design and thus the importance of getting the optical design and engineering right.

Subsequent investigations focused on solid-state LSC designs and light-management strategies to improve the coupling efficiency. In 2021, Dottermusch et al. analyzed several solid-state LSC-based configurations through ray-tracing simulations, predicting up to a seven-fold enhancement in gain coefficient and a 30-fold increase in laser output power relative to earlier liquid-state LSC technologies [19]. Further optimization studies using *LightTools* simulations explored cavity improvements through separation of the fiber and sensitizer, introducing new solid-state geometries for enhanced light confinement [20]. The experimental realization of these concepts was reported in 2023 [21], where a planar SPFL with a 30 cm aperture produced 15 mW output, corresponding to a solar-to-laser efficiency of 0.023% and a collection efficiency of 0.21 W/m^2—representing a 12-fold improvement over earlier liquid-LSC designs.

Finally, the most recent experimental study [22], which represents the current state-of-the-art in planar SPFL configurations, demonstrated further performance enhancement through improved photon confinement and sensitization. The perhaps-surprising number of components in the SPFL comes down to one inescapable fact: that the optical losses in the system are large. Here, the optical losses were minimized by sandwiching the LSC between a frontal dichroic mirror (DM_{front}) and a rear dichroic mirror (DM_{rear}), with a polytetrafluoroethylene (PTFE) ring acting as a Lambertian reflection around the edges. The sensitization film within the LSC consisted of a mixture of two commercial perylene dyes (Lumogen series, BASF, Germany) – 0.39 mg/g of Orange 240 (O240) and 0.79 mg/g of Yellow 083 (Y083)—dissolved in a fluoropolymer host, which yields relatively broadband absorption (350 nm–600 nm) and emits at a peak of 580 nm with a photoluminescence quantum yield (PLQY) of 90%. As a result, a slope efficiency of 0.1% and an output power of 34 mW were achieved in a fully planar SPFL with a 30 cm aperture and a fiber length of 400 m.

Analysis of studies conducted over the past decade reveals clear evolutionary patterns and incremental advances in the development of sensitizer-assisted SPFLs. The overall solar-to-laser slope efficiency has improved by approximately 28-fold, increasing from an initial value of 0.0036% [14] in 2017 to the current state-of-the-art value of about 0.1% [22] in 2024. This progress can be attributed to the exploration of various system configurations and sensitizer materials that help reduce optical losses within the system. A consistent trend indicates that increasing the active fiber length enhances laser performance, with reported lengths growing from approximately 40 to 400 m over time. Furthermore, the lasing threshold has been significantly reduced, with lasing now occurring at input solar powers of 30–40 W for a 400 m fiber. These studies also highlight the critical influence of both sensitizer properties and photon-confinement cavity design. Finally, thermal effects have been consistently identified as a major factor influencing system performance, underscoring the need for active cooling (e.g., via a Peltier device) to achieve lasing [15, 22].

Despite substantial effort and progress in planar one-sun SPFLs, currently their overall performance remains low [22], particularly in comparison with solid-state SPLs operating under concentrated sunlight [6]. The latest SPFL experimental demonstrations report solar-to-laser conversion efficiencies on the order of ≈0.05%. This performance is determined by the combined action of several tightly coupled processes, including photon confinement, spectral conversion, fiber-scale absorption, and gain-lasing dynamics. In systems of this degree of complexity, partially simplified theoretical treatments can obscure the mechanisms that ultimately limit efficiency, particularly when multiple loss channels act simultaneously. As a result, identifying the truly performance-limiting mechanisms becomes challenging, since loss channels that appear dominant in magnitude may in fact be amplified by more fundamental underlying mechanisms within the coupled optical system.

To address this challenge, a central goal of this work is the development of a validated physics-based digital twin of a SPFL experimental system, constructed to reproduce the geometric architecture of the cavity as closely as possible and grounded in experimentally measured optical and material properties of each system component. By reproducing measured quantities such as small-signal gain and laser output, while modeling photon transport, spectral conversion, fiber-level interaction processes, and thermal effects, the model enables detailed element-wise analysis of the cavity. This framework makes it possible to disentangle competing loss mechanisms and identify performance-limiting effects that are not directly apparent from experimentally measured global performance metrics alone. Importantly, it also provides a systematic framework for exploring alternative cavity schemes, fiber parameters, and fiber arrangements. Building on this validated model, we investigate alternative pumping and confinement strategies aimed at improving photon–core interaction efficiency. These optical-engineering studies are guided directly by insights obtained from the digital twin, enabling systematic evaluation of configurations with the potential to improve performance relative to current state-of-the-art SPFL implementations.

2 | Planar Solar-Pumped Fiber Laser Model

It is important to clarify that the present work builds upon previous SPFL modelling efforts reported in the literature [16, 19, 20]. In [16], a model was developed that demonstrated good predictive capability in capturing general performance trends. The subsequent studies [19, 20] employed the LightTools simulation environment, which provided valuable insights for designing, but, due to the non-transparent implementation principle of this software, it inherently limits detailed, process-level ("surgical") analysis of photon behavior within the system. In the mentioned studies, the volume containing the fiber coils was treated as an effective medium characterized by a scattering coefficient. Although this constitutes a convenient first-order approximation, it can reduce accuracy under certain conditions and obscure the physical mechanisms governing photon transport and coupling efficiency. In the earlier studies [10, 20], laser output was estimated using a scalar rate-equation approach, which, although adequate at low gain levels, does not provide a complete description of fiber-laser performance. More generally, while simplified analytical relations are useful for identifying individual scaling trends, the pump rate in the present LSC-assisted SPFL emerges from coupled wavelength-, angle-, and geometry-dependent photon transport through the sensitizer, confinement cavity, and coiled fiber. A compact relation between laser output power and parameters such as core diameter, cavity loss, and output coupling would therefore require substantial averaging of these coupled processes. The present model instead treats the fiber coil explicitly and couples Monte Carlo ray tracing to the rate and power-propagation equations. Analytical estimates are used for isolated processes, such as single-pass sensitizer and fiber-core absorption. Together, these refinements provide a more physically representative description of the system, enabling identification

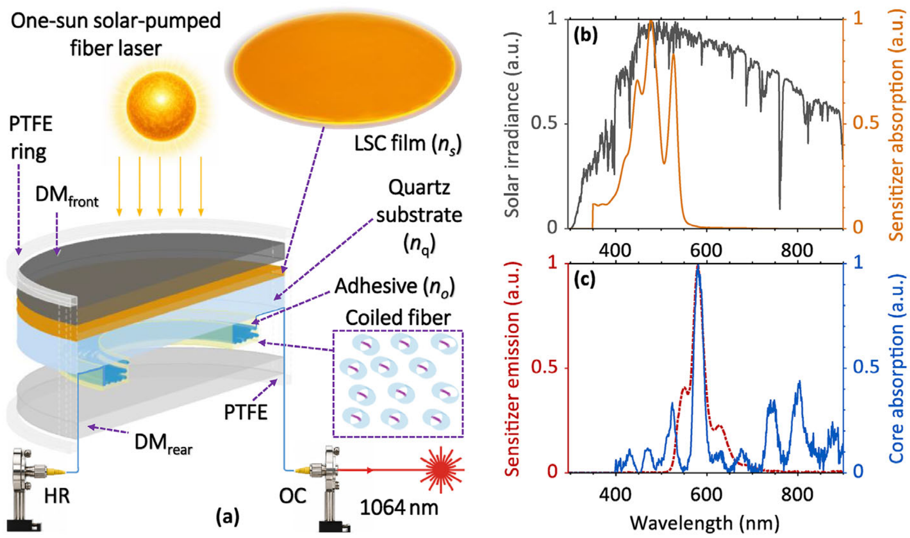

FIGURE 1 | SPFL model elements and their spectral data. (a) Schematic representation of the SPFL, where HR denotes the high reflector (HR) and OC the output coupler (OC). (b) Solar spectral irradiance and the absorption spectrum of the dye-doped polymer sensitizer film. (c) Emission spectrum of the sensitizer film (measured at the edge of the LSC) and absorption spectrum of the Nd^{3+}-doped fiber core. Spectra are normalized to their respective peak values for clarity.

of the mechanisms constraining performance and offering deeper insight into possible design improvements.

2.1 | Monte Carlo Ray-Tracing Model of a Photon Confinement Cavity

The present model is developed and evaluated using the experimental results from the latest study [22] together with the measured fiber-core parameters reported in [15], which collectively provide the essentials for validation. The following section briefly describes each component of the planar photon-confinement system, outlining its functional role and its representation within the model. Where relevant, uncertainties and limitations in the available experimental data—such as incomplete refractive-index information or limited spectral and angular characterization of optical components—are also noted, as these factors may influence modeling accuracy.

2.1.1 | Photon Confinement Cavity Description

The schematic diagram in Figure 1a presents a schematic of the photon-confinement cavity implemented in the simulation model, constructed to closely replicate the experimental configuration reported in [22]. In brief, the structure consists of (from top to bottom):

i. DM_{front}—designed to allow excitation light up to 570 nm to pass through to the LSC, while preventing luminescence (peak at 580 nm) escaping out of the top surface (see Supplementary Information of reference [23] for details);

ii. an air gap is required to allow the LSC to maintain total internal reflection;

iii. the thin-film LSC is formed by an ≈80 μm-thick sensitizer layer, which is doctor-blade coated onto a double-side-polished quartz substrate (1 mm thick, 30 cm in diameter with refractive index, n_q) (see Supplementary Information [23] for details);

iv. the Nd^{3+}-doped optical fiber coil is then bonded to the lower surface of the quartz plate;

v. an additional air gap is required below the LSC to maintain total internal reflection;

vi. DM_{rear}, similar in function to the DM_{front}, to prevent the escape of luminescence peaked at 580 nm;

vii. the entire assembly is radially enclosed by a cylindrical PTFE ring that provides optical confinement via diffuse reflection;

viii. a final component, not shown here, is a Peltier cooling plate used to reduce the operating temperature to −45°C.

Operation is as follows: in this configuration, incident solar photons enter the system through the DM_{front}, which selectively transmits the relevant portion of the solar spectrum. The transmitted photons first interact with the sensitizer film, where they are absorbed and subsequently re-emitted at wavelengths centered around 580 nm. The combined structure of the sensitizer film and quartz substrate functions as an LSC, guiding the re-emitted photons toward the fiber coils. Both the DM_{front} and DM_{rear} are designed to maintain high reflectivity within the 580 nm spectral band over a broad range of incidence angles and polarizations. The surrounding PTFE ring further contributes to photon confinement within the cavity through diffuse scattering.

2.1.2 | Mirror and Outer Confinement Modeling

The outer confinement structure consists of a DM_{front} and a DM_{rear}, both modeled as coated mirrors with wavelength-dependent reflectivity over the 350–900 nm range. Reflectivity is defined as a function of polarization (s and p) and incident angle, with the manufacturer's data plotted in Supplementary Information [23] being available only at discrete angles (0–89° in 10° increments). The surrounding PTFE ring is modeled as a 99% diffuse reflector.

2.1.3 | Sensitizer Film Modeling

The sensitizer layer is modeled as a cylindrical film with a diameter of 30 cm and a thickness of 80 µm. The fluorinated polyurethane host consisted of Lumiflon LF 910LM and Duranate, incorporating Lumogen F Orange 240 (O240) and Lumogen F Yellow 083 (Y083) dyes. The dye loadings were 7.0 mg O240 and 7.07 mg Y083 per 10.0 g of Lumiflon, corresponding to approximately C_{O240} = 0.70 mg g^{-1} and C_{Y083} = 0.707 mg g^{-1} with respect to Lumiflon, respectively. The optical density at 532 nm was 0.6 [22, 23]. The refractive index of the composite film was measured previously to be 1.47 at 637 nm [19]; therefore, this non-dispersive value of n_s = 1.47 was adopted in the model. The measured absorption spectrum (plotted in Figure 1b for comparison with the solar spectrum to highlight the spectral overlap relevant for absorption) and emission spectrum (plotted in Figure 1c for comparison with the Nd^{3+}-doped fiber core [24] absorption spectrum) were directly implemented in the ray-tracing model. The film absorbs photons in the 350–550 nm range and re-emits them around 580 nm, with a measured photoluminescence quantum yield (PLQY) of 90% ± 3% [22].

2.1.4 | Fiber Coil Geometry and Representation

A significant modeling challenge arises from the geometry and arrangement of the fiber coils. In the experiment, a 400 m fiber (Furukawa Denko Corporation, Japan)—comprised of a 16 µm aluminosilicate fiber core doped with 0.5% Nd^{3+} and a silica cladding bringing the total outer diameter to 125 µm (the original outer polymer cladding was removed)—was manually bonded to the underside of a glass substrate using an optical adhesive, forming a shallow trough-like structure with irregular positioning of the fibers. As previously mentioned, earlier models approximated this component as an effective scattering medium characterized by a tunable scattering coefficient. In contrast, in the present work, the fiber is modeled explicitly. The coil geometry is generated numerically around an average radius, with small random perturbations applied sequentially to each turn to emulate experimental irregularities. The resulting structure consists of approximately 600–700 toroidal turns representing the full 400 m fiber length. Because the fiber diameter is on the micrometer scale while the overall cavity dimensions are on the centimeter scale, individual coils are not visible in the full system view. Therefore, the inset image within Figure 1a presents a zoomed-in cuboidal section directly extracted from the model, highlighting the randomized fiber arrangement.

2.1.5 | Optical Adhesive

Following the work of [20], the optical adhesive was assumed to be Norland Optical Adhesive 85 (NOA 85). The nominal refractive index was taken as n_o = 1.48, consistent with the manufacturer's technical data sheet [25]. In addition, a range of refractive indices (n_o = 1.42 – 1.50) was explored in the model (see Section 4.2) to assess the sensitivity of the results to this parameter.

2.2 | Validation of the Monte Carlo Ray Tracing Model

The primary objective of the Monte Carlo ray-tracing model is to quantify the optical power absorbed within the fiber core and to resolve the photon-flow distribution throughout the entire cavity. Thus, the model is developed to provide spatial and statistical insight into photon transport, confinement efficiency, and loss channels within the system. A critical question, however, concerns the validation of the model. Direct validation through comparison with laser output represents the ultimate test. However, laser operation is governed by multiple coupled processes including gain dynamics, amplified spontaneous emission (ASE), background losses, and thermal effects making it difficult to isolate potential shortcomings arising solely from the pumping model, that is Monte Carlo ray tracing. To reduce parameter space, the experimentally reported single-pass differential gain of the SPFL in [22, 23] was utilized as an intermediate validation metric. The single-pass differential gain is primarily determined by the absorbed pump power within the fiber core and stimulated emission cross sections, which is less influenced by cavity feedback, ASE evolution, or scattering losses. As such, it provides a more direct and less ambiguous benchmark for assessing the accuracy of the ray-tracing model.

The principal assumptions and approximations adopted in the Monte Carlo ray-tracing model are described here. The wavelength-dependent refractive indices of the sensitizer film, and optical adhesive. As mentioned, reflectivity data for the DM_{front} and DM_{rear} were only available at discrete incidence angles (0–89° in 10° increments). Thus, in the simulation, the incident angle of each ray is explicitly calculated and the corresponding reflectivity assigned according to the nearest tabulated angular interval. The experimentally realized fiber–substrate interface, formed by manual bonding of the fiber to the quartz plate, exhibits surface irregularities. In the model, this interface is approximated using planar segments around the fiber bundle, with roughness represented through a microfacet formulation based on an isotropic Gaussian distribution of surface slopes. Finally, the PLQY of the sensitizer film is reported [22] to be 90% ± 3%.

Having established the model formulation and assumptions, the resulting photon transport and absorption characteristics of the system were analyzed. Sampled solar photons are traced throughout the cavity, and the absorption efficiency in the fiber core is quantified using two complementary metrics: a photon-count-based efficiency $\mu_{count} = N_{abs} / N_{pumped}$, and an energy-based efficiency $\mu_{energy} = \sum E_{abs} / \sum E_{pump}$. The developed model demonstrated good numerical convergence of the Monte Carlo simulation, as the calculated absorption efficiency converged beyond approximately 1×10^5 traced photons (Figure 2a). A more detailed discussion of the simulation results is provided in Section 3 after establishing the validity of the model.

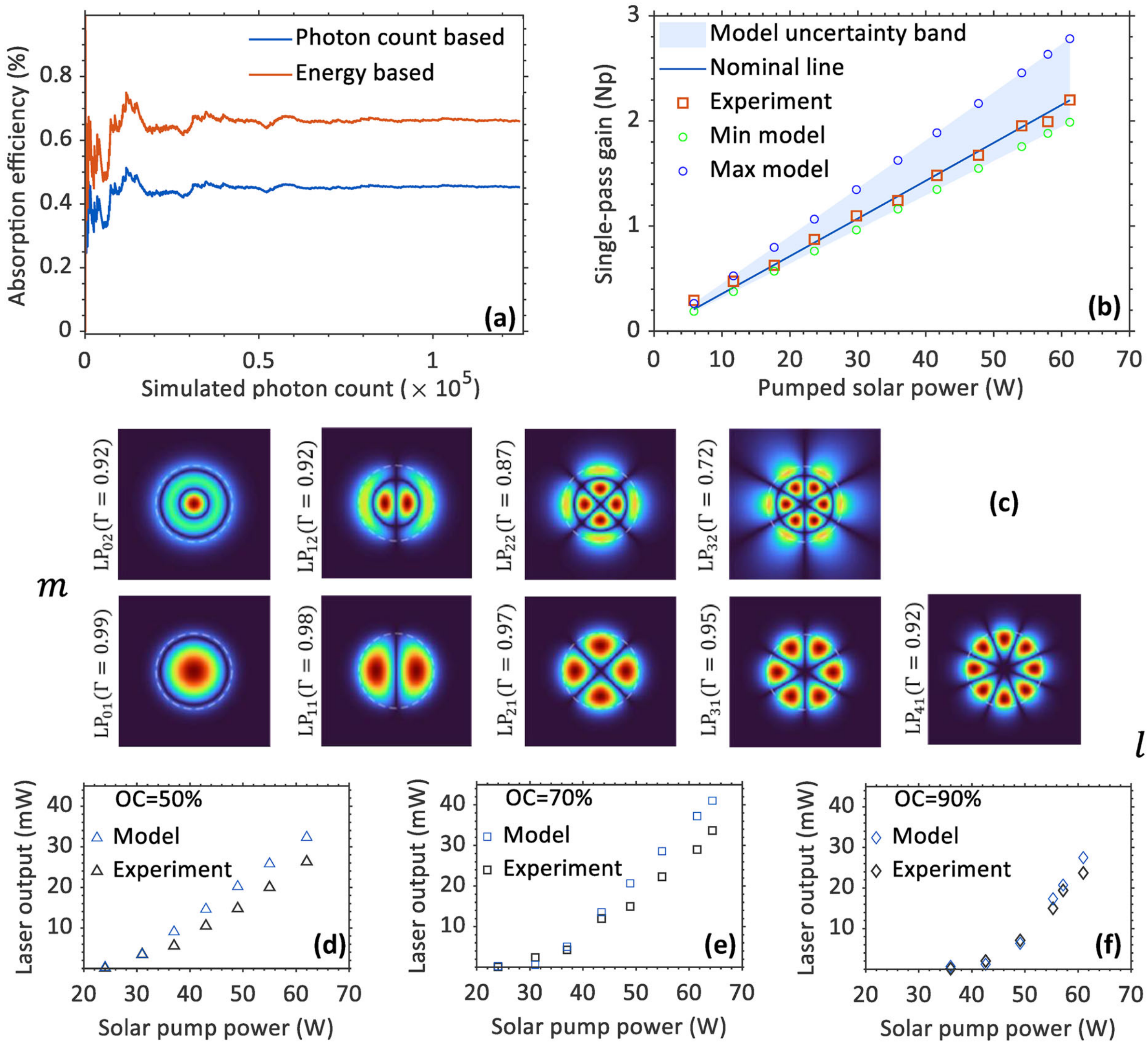

FIGURE 2 | Validation of the model. (a) Absorption efficiency and its convergence behavior as a function of the number of simulated photons. (b) Comparison of measured and simulated single-pass small-signal gain. (c) Linearly polarized (LP) spatial modes supported by the fiber and their mode–gain overlap coefficients. (d,e,f) Comparison of modeled and measured laser output for different output coupler transmittances.

The accuracy of the model predicted absorption range with experimental observations was evaluated by computing the corresponding small-signal gain and comparing it with the measured data reported in [23]. In the experiment [23], a probe signal from a superluminescent diode is injected into the fiber, and the transmitted spectrum is recorded under three conditions: $A(\lambda)$—probe + solar (outside) illumination, $B(\lambda)$—probe only (no solar pumping) and $C(\lambda)$—solar illumination only (spontaneous emission). The spontaneous emission background is subtracted from the probe-under-sunlight signal, and the single-pass differential gain is defined as:

$$G(\lambda) = (A(\lambda) - C(\lambda)) / B(\lambda) \quad (1)$$

with $G(\lambda) = e^{\gamma_0 l}$, where γ_0 is the small-signal gain coefficient and l is the fiber length. Figure 2b presents the comparison, with the red squares represent experimentally measured data extracted from [23], while the green and blue circles correspond to model predictions based on absorption efficiencies of $\mu_{energy} = 0.48\%$ and $\mu_{energy} = 0.66\%$, respectively. The nominal case corresponding to 0.54% absorption efficiency (PLQY = 87%) shows closer agreement with the experimental data. Subsequent analysis and discussion are therefore based on this validated configuration.

2.3 | Digital Twin of Planar Solar Pumped Fiber Laser: Fiber Laser Output Modelling

Once the pumping characteristics are established through Monte Carlo ray-tracing analysis, the resulting lasing dynamics can be modeled. For the estimation and analysis of fiber laser output, two principal modeling approaches are widely used in the literature: (i) scalar rate equations, typically applied under moderate gain conditions when the primary interest lies in the global population-inversion dynamics, such as predicting lasing threshold and overall output power with sufficient accuracy [26]; and (ii) coupled rate and power propagation equations, which provide a more comprehensive description of the system [27]. The coupled rate and power propagation equations framework remains the standard for fiber laser modeling, offering higher accuracy and captures multiple physical effects without relying on simplifying assumptions, such as those involving transverse gain–mode overlap coefficients.

Here, the implementation of the coupled rate and power propagation equations framework begins with the analysis of the linearly polarized (LP) spatial modes supported by the fiber. As in the experiment [22], the fiber used in the model has a step-index, circular geometry with a cladding diameter of 125 and a 16 µm Nd^{3+}-doped aluminosilicate core. The numerical aperture (NA) is 0.18, defined as $NA = \sqrt{n_{core}^2 - n_{clad}^2}$. The refractive indices used in the model were determined based on the fact that the fiber cladding consists of pure silica, with corresponding data taken from [28]. The core refractive index is calculated via NA relation, $n_{\text{clad}} = 1.45$ and $n_{\text{core}} = 1.461$ at 1064 nm.

The normalized frequency (V-number) of the fiber was calculated using, $V = 2\pi rNA/\lambda$, which yielded a value of 8.09. Since this value is well above the single mode cut-off of 2.405 [29], the fiber used in the experiment should be considered multimode. Accordingly, the LP spatial modes supported by the fiber were analyzed, and their mode–gain (assuming gain is uniform across the fiber) overlap coefficients were calculated [29]. Figure 2c presents the nine dominant modes identified in this fiber along with their corresponding overlap coefficients.

The propagation of optical powers and the steady-state populations in the Nd^{3+} -doped fiber core are described using one-dimensional coupled equations, as follows. In the present quasi-three-level model, $N_2(z)$ denotes the population density of the $^4F_{3/2}$ upper laser manifold, while $N_1(z)$ denotes the thermally populated $^4I_{11/2}$ lower laser manifold for emission near 1064 nm. The lower-level population is calculated as $N_1(z) = f_T(T)[N_{\text{tot}} - N_2(z)]$, where $f_T(T)$ is the thermal population fraction determined from the $^4I_{9/2}$ and $^4I_{11/2}$ Stark levels following [15]. The population densities are expressed in $ions/m^3$. The forward and backward powers of the i^{th} guided signal mode, $P_{s,i}^+(z)$ and $P_{s,i}^-(z)$, satisfy:

$$\frac{dP_{s,i}^{+}(z)}{dz} = \left[\Gamma_{s,i}\left(\sigma_e(\lambda_s)N_2(z) - \sigma_a(\lambda_s)N_1(z)\right) - \alpha_s\right] P_{s,i}^{+}(z), \tag{2}$$

$$\frac{dP_{s,i}^{-}(z)}{dz} = -\left[\Gamma_{s,i}\left(\sigma_e(\lambda_s)N_2(z) - \sigma_a(\lambda_s)N_1(z)\right) - \alpha_s\right] P_{s,i}^{-}(z) \tag{3}$$

where $\Gamma_{s,i}$ is the confinement (overlap) factor of mode i with the doped region, σ_e and σ_a are the emission and absorption cross sections at the signal wavelength λ_s, and α_s represents background/intrinsic losses at λ_s.

ASE is discretized into spectral bins b (center frequency ν_b , bandwidth $\Delta\nu_b$) and guided spatial modes m. The forward and backward ASE powers $P_{\text{ASE},m,b}^{+}(z)$ and $P_{\text{ASE},m,b}^{-}(z)$ obey:

$$\frac{dP_{\text{ASE},m,b}^{+}(z)}{dz} = \left[\Gamma_{m,b}\left(\sigma_{e,b}N_2(z) - \sigma_{a,b}N_1(z)\right) - \alpha_{m,b}\right] P_{\text{ASE},m,b}^{+}(z) + 2\Gamma_{m,b}\sigma_{e,b}N_2(z)\, h\nu_b\Delta\nu_b, \tag{4}$$

$$\frac{dP_{\text{ASE},m,b}^{-}(z)}{dz} = -\left[\Gamma_{m,b}\left(\sigma_{e,b}N_2(z) - \sigma_{a,b}N_1(z)\right) - \alpha_{m,b}\right] P_{\text{ASE},m,b}^{-}(z) - 2\Gamma_{m,b}\sigma_{e,b}N_2(z)\, h\nu_b\Delta\nu_b \tag{5}$$

where $\sigma_{e,b} = \sigma_e(\nu_b)$ and $\sigma_{a,b} = \sigma_a(\nu_b)$. The factor $\Gamma_{m,b}$ is the overlap factor of ASE mode m with the doped region at frequency bin b, and $\alpha_{m,b}$ denotes background loss (optionally wavelength/mode dependent). The factor of 2 accounts for two orthogonal polarization states. The steady-state upper-level population is determined from the balance between the pump, signal, and ASE transition rates as:

$$N_2(z) = \frac{R_p(z)}{\sum_i W_{s,i}(z) + \sum_b W_{\text{ASE},b}(z) + 1/\tau}, \tag{6}$$

where $W_{s,i}$ and $W_{\text{ASE},b}$ are the stimulated transition rates induced by signal and ASE fields, respectively and τ is the PL lifetime.

To solve the coupled rate and power propagation equations, it is necessary to specify the lasing characteristics of the fiber core. A detailed study of these properties for the same type of Nd^{3+}-doped aluminosilicate fiber was reported by Bisson et al. [15], thus the emission and absorption cross-sections as well as the background loss values were taken directly from that work. Since thermal effects are known to be significant under weak pumping conditions, the energy-level data of the active ions required for thermal analysis were adopted from [30]. A summary of the used parameters in the model is provided in Table 1.

The experimental study [22] reported laser output measurements for output coupler (OC) transmittance values of 50% (Figure 2d), 70% (Figure 2e) and 90% (Figure 2f) with the pumping power increased incrementally by adjusting the illuminated area of the cavity aperture. OC and HR—feedback mirrors in this fiber laser are assumed to have 1.6% loss per fiber-mirror connection [31]. A point-by-point comparison between the modeled results obtained by combining the Monte Carlo ray-tracing pumping analysis with the coupled rate and power propagation equations and the experimentally measured data (extracted from [22]) is presented in Figure 2d–f. The model reproduces the measured output characteristics with excellent quantitative agreement, especially when using the OC with 90% reflectance (Figure 2f). Deviations become noticeable at higher circulating powers, particularly for larger OC reflectivity. In the present implementation, the absorbed pump power within the fiber core is assumed to be axially and radially uniform. The axial component of this approximation is supported by the very low single-traversal absorption probability of the 16 µm core, which makes local pump depletion by individual fiber turns negligible, and by Monte Carlo ray traying evaluation along the 400 m fiber, which revealed no systematic over- or under-pumped regions beyond statistical fluctuations Nevertheless, unresolved local and radial variations may contribute to the remaining discrepancies. The model captures the dominant trends in threshold behavior and output scaling, supporting its physical consistency and its use as a validated digital representation of the planar SPFL system. The present framework is intended for the experimentally investigated one-sun operating regime, for which the agreement with measured laser output indicates that neglected nonlinear effects such as stimulated Brillouin or Raman scattering and

TABLE 1 | Parameters used in the laser SPFL model.

Parameter name	Used value	Refs.
Laser wavelength	1064 nm	[22]
Pump wavelength	580 nm	[22]
Nd^{3+} excited state lifetime	450 μs	[15]
Effective simulated emission cross section[a]	1.2×10^{-24} m^2	[15]
Effective re-absorption cross section[a]	0.57×10^{-24} m^2	[15]
Background loss of fiber	1.25 / km	[15]
Nd^{3+} doping concentration	1.3×10^{20} at./cm^3	[15]
Operating temperature	233 K	[22]
Resonator mirror: Pigtail output coupler	50,70,90%[b]	[22, 31]
Pigtail high reflector	100%[b]	[22, 31]
Pump quantum efficiency[c]	95%	[32]

[a]At room temperature.
[b]A loss 1.6% (= 0.07 dB) loss per fiber-mirror connection is assumed.
[c]The pump quantum efficiency is assumed to be 95%.

Kerr-related phenomena are not dominant. At substantially higher irradiance or intracavity power, the model would require extension to include nonlinear propagation effects. Therefore, in the following section, the model is employed to investigate performance-limiting mechanisms and explore alternative design configurations.

3 | Photon-Flux Analysis of the Pumping Cavity

Having established agreement between the model and experimental laser output, the validated framework can now be used to examine the internal photon dynamics of the pumping cavity. Unlike experimental measurements, which provide only aggregate output metrics, the SPFL digital twin developed here enables direct access to photon-flux distributions, absorption pathways, and loss channels throughout the system. This section presents a detailed photon-flux analysis aimed at identifying the dominant mechanisms that limit pumping efficiency.

The power-based Sankey diagram in Figure 3 illustrates the progression of incident solar energy (100%) in the air-mass 1.5 global (AM1.5G) spectrum via successive optical processes, indicating the relative distribution of losses and confinement within the cavity. Approximately 39.5% of the incoming solar irradiance is spectrally mismatched and therefore cannot be absorbed by either the sensitizer layer or the fiber core directly, leaving 60.5% spectrally useful—that is, associated with a non-zero absorption coefficient. Of this portion, 34.2% is lost at the initial entrance through DM_{front} due to wavelength-dependent transmission. The remaining 26.2% is successfully confined and available for interaction within the cavity.

Within the confined fraction, photons experience losses through several mechanisms. Intrinsic conversion losses in the sensitizer account for 9.1%, arising from non-unity PLQY ≈ 0.87. Additional losses occur due to imperfect diffuse reflection at the PTFE boundary (1.1%), as well as escape from the cavity through reflectivity of the front and rear mirrors: 6.3% through DM_{rear} and 6.8% through DM_{front}, primarily due to wavelength- and incident angle-dependent transmission. Ultimately, 0.54% of the total incident solar power is absorbed within the fiber core, representing the fraction that contributes to population inversion and laser excitation.

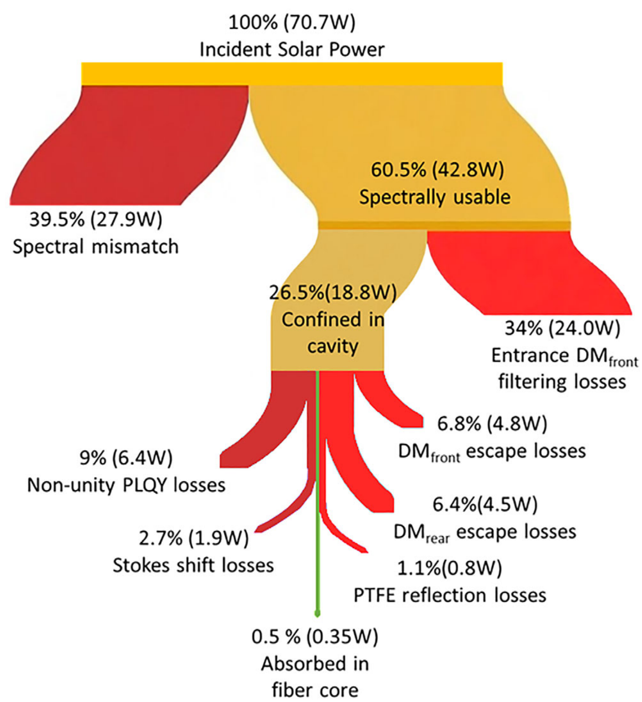

FIGURE 3 | Photon-flow distribution in the modeled planar SPFL cavity for a representative simulation case, illustrating the relative distribution of optical power and loss mechanisms.

The Sankey diagram provides a global distribution of incident solar power within the optical system, indicating that material-related losses account for approximately 51.2% (comprising spectral mismatch 39.5%, non-unity PLQY losses 9%, and

Stokes shift losses 2.7%), shown in dark red, whereas cavity-related losses associated with imperfect photon confinement account for approximately 48.3%, represented by lighter red shades. However, the diagram does not resolve the underlying physical mechanisms responsible for these losses. The following section therefore examines each cavity component individually to identify the dominant processes limiting pumping and lasing performance.

3.1 | Dichroic Mirror Performance Trade-Offs

The Sankey diagram features two loss channels associated withDM$_{front}$: "entrance DM$_{front}$ filtering losses" and "DM$_{front}$ escape losses," which together account for a total loss of 40.8%. These loss channels are discussed separately.

For the analysis of initial filtering losses, the full incident solar spectrum was considered, including spectrally mismatched photons. To quantify the initial influence of the DM$_{front}$, a simple power estimate was performed. Suppose that the entrance aperture (30 cm diameter) receives approximately 70.7 W of optical power under an irradiance of 1000 W/m^2. The DM$_{front}$ reflectance and transmittance are specified over the wavelength range 350–1000 nm, which encompasses the relevant spectral region for both the sensitizer and the fiber core. Within this interval, 51.4 W of the incident power 70.7 W is contained; however, after transmission through the DM$_{front}$ at normal incidence, only 20.9 W transmitted into the cavity. Due to its spectral design, DM$_{front}$ suppresses the direct contribution of three major fiber-core absorption bands at 580 nm (corresponding to $^4G_{5/2}$ and $^2G_{7/2}$ energy level transitions of Nd^{3+} ions), 745 nm ($^4S_{3/2}$ and $^4F_{7/2}$), and 808 nm ($^4F_{5/2}$ and $^2H_{9/2}$). Excitation of the fiber core therefore relies predominantly on radiative transfer via the sensitizer. This behavior is a direct consequence of the system design. In addition, the suppressed absorption bands at longer wavelengths are weaker than the 580 nm band, further reinforcing the dominance of sensitizer-mediated excitation.

To understand the origin of DM$_{front}$ escape losses, the transmitted solar spectrum and the DM$_{front}$-reflected spectrum at the cavity-facing surface were analyzed. For this purpose, the spectral range 350–750 nm was considered, as it encompasses the radiation circulating within the cavity that can potentially contribute to sensitizer absorption and subsequent emission. Figure 4a shows the spectral distribution of photons escaping through the DM$_{front}$ (red) and the reflected spectrum (green), both computed within the simulation, together with the band (wavelength)-averaged reflectivity of the DM$_{front}$ over the 350–750 nm range (purple), derived from the manufacturer's data [23]. It can be seen that the escape losses span the wavelength range from 350 to 750 nm. In particular, the 350–550 nm region corresponds to solar photons that would otherwise be absorbed by the sensitizer, while the 550–570 nm region overlaps with the sensitizer emission band.

Overall, these results show that DM$_{front}$ escape losses include both unabsorbed solar photons by the sensitizer and a non-negligible fraction of sensitizer-emitted radiation, which would otherwise contribute to photon recycling within the cavity. In

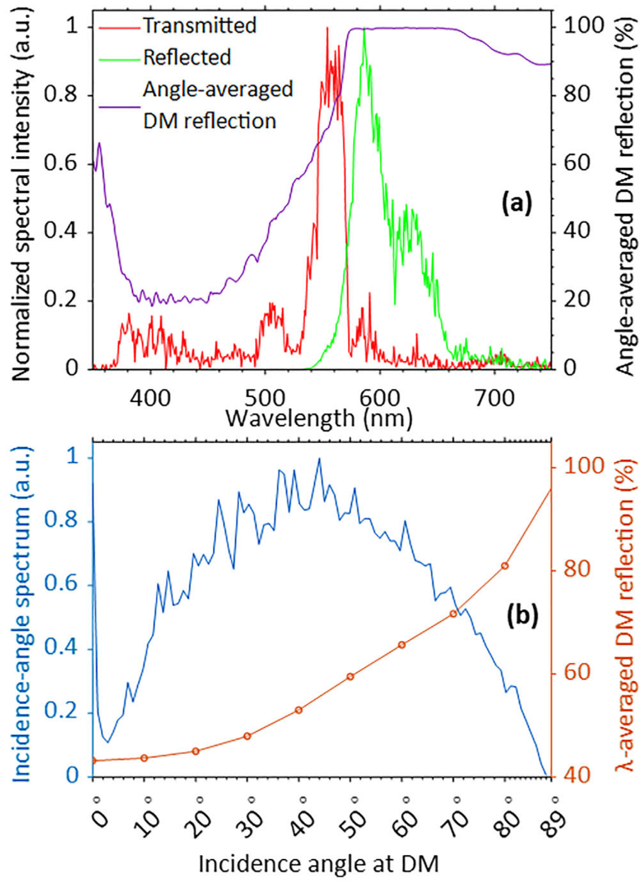

FIGURE 4 | (a) Spectral distribution of photons interacting with the dichroic mirror, together with angle-averaged reflectivity of the mirror (purple). (b) Angular distribution of photon incidence at the DM for all photons within the cavity, together with the reflectivity wavelength-averaged over the 350–750 nm emission range.

addition to spectral effects, the angular dependence of the DM reflectivity plays a critical role in photon confinement. Although solar radiation enters the cavity at near-normal incidence (design angle $\approx 0°$), scattering within the sensitizer and reflections from the fiber coils lead to a broad angular redistribution of photons. As a result, photons impinge on the cavity-facing surface of the DM$_{front}$ over a wide range of angles rather than remaining near normal incidence. This behavior is directly observed in the simulation and shown in Figure 4b which presents the angular distribution of photon incidence at the DM$_{front}$ for the full cavity spectrum, together with the reflectivity averaged over the 350–750 nm relevant spectral range for pumping. Consequently, the commonly assumed near-normal incidence condition does not hold within the cavity, and angular-dependent reflectivity cannot be neglected. The angular spread of photons therefore plays a key role in limiting photon confinement and directly contributes to the ≈6.8% escape losses attributed to the DM$_{front}$ in the Sankey diagram.

As with the DM$_{front}$, the reflectivity of the DM$_{rear}$ exhibits strong angular dependence. Photons incident at oblique angles experience reduced reflectivity, leading to cumulative angular losses over multiple reflections. Similarly, ≈6.4% escape losses attributed to the DM$_{rear}$ in the Sankey diagram.

3.2 | Sensitizer Film

As previously mentioned, the 80 µm-thick sensitizer film forms the active layer of the LSC, with the fiber bundle—the "receiver" in the SPFL system—adhered onto the opposite side of the 1mm-thick quartz substrate. The key question addressed here is the effectiveness of solar-photon sensitization within this configuration. The DM_{front}–LSC–DM_{rear} structure implicitly assumes that light entering the LSC is absorbed efficiently and re-emitted within the spectral range accessible to the fiber core. If single-pass absorption is incomplete, unabsorbed photons remain susceptible to leakage through the DM_{rear} or DM_{front} after a double pass. To quantify this behavior analytically, an idealized single-layer LSC is considered, and the single-pass solar absorption is calculated by accounting for the 80 µm thickness, normal incidence, measured absorption spectrum, and Fresnel reflections. The absorbed power is expressed as:

$$\boldsymbol{P}_{abs} = \int_{\lambda min}^{\lambda max} [S(\lambda) \times [1 - R_{\mathrm{DM}}(\lambda)]] \times [1 - R_{\mathrm{Fresnel}}(\lambda)] \left(1 - e^{-\alpha(\lambda) L}\right) d\lambda \quad (7)$$

In this expression, the first term inside the integral represents the solar spectrum, the second term transmission through the DM_{front}, the third accounts for Fresnel reflection losses at the interface, and the fourth describes absorption within the LSC layer. Using relevant parameters, approximately 20.88 W is transmitted through the DM_{front} into the cavity. Of this, 9.4 W (≈45%) is absorbed in a single pass through the 80 µm sensitizer layer, while 11.5 W (≈55%) remains unabsorbed. These results indicate that single-pass absorption is incomplete under the current thickness. However, modifying the LSC thickness also alters photon dynamics within the cavity, including reabsorption processes and PLQY, and therefore affects overall sensitization efficiency. This interplay is examined in more detail in Section 4.2 that follows. Importantly, thickness variation represents a geometric optimization. Additional improvements may be achieved at the material level, for example by increasing PLQY or selecting sensitizers with improved spectral alignment to both the solar spectrum and the fiber-core absorption bands [33].

3.3 | Fiber Coils

Efficient excitation of the fiber core requires repeated photon traversals, as the single-pass absorption probability is inherently limited by the 16 µm core diameter. To quantify this constraint, consider the Beer–Lambert relation:

$$A_{\mathrm{abs}} = 1 - e^{-\alpha L} \quad (8)$$

where A_{abs} is the absorption probability and α is the absorption coefficient (cm^{-1}) and L is the optical path length (units: cm) through the core. For the spectral region corresponding to the LSC emission near 580 nm, the absorption coefficient of the core reaches approximately 3–4 cm^{-1} (its maximum value among four main absorption peaks). Substituting $L = 16 \times 10^{-4} cm$ yields $A_{\mathrm{abs}} = 1 - e^{-3.5\times16\times10^{-4}} \approx 5.6 \times 10^{-3}$, i.e., a 0.56% probability. Although small, this value confirms that a single traversal contributes only marginally to excitation. Solving the inverse Beer–Lambert relation for a target absorption probability of 0.9, $L = -\ln(1 - 0.9)/\alpha \approx 0.658$ cm. This corresponds to more than 400 effective core traversals. Such a requirement imposes stringent constraints on optical confinement efficiency. For illustration, consider a surface with a reflectivity of 99%. After 400 reflections, the surviving fraction becomes $0.99^{400} \approx 0.018$, meaning that only about 1.8% of the optical power remains while 98.2% is lost. In contrast, a reflectivity of 99.9% would allow for 67.0% of photons to remain after 400 reflections. These estimates highlight the extreme sensitivity of the system to even modest confinement imperfections.

To further examine photon–fiber interaction within the validated Monte Carlo ray-tracing framework, the distribution of ray–fiber intersection events was quantified by recording, for each photon in the cavity, the number of crossings through both the fiber cladding and core regions. Considering the total photon population confined within the DM_{front}–PTFE–DM_{rear} structure, only $A(L_{\mathrm{core}} > 0) =$ 17.2% of photons intersect the fiber core at least once, whereas 82.8% never traverse the core. This behavior results from multiple loss mechanisms and geometric constraints, including limited PLQY, reabsorption in the sensitizer, and leakage through the DM_{front}, DM_{rear} and PTFE boundaries. From an optical pathlength perspective, the mean cumulative pathlength inside the fiber core for all cavity photons is $\langle L_{\mathrm{core}} \rangle = 5.8 \times 10^{-3}$ cm, calculated within the model. Applying the Beer–Lambert relation, $A_{\mathrm{abs}} = 1 - e^{-3.5\times5.8\times10^{-3}} \approx 0.02$, indicating that approximately 2% of all cavity photons (according to the Sankey diagram, it was 26.5%) are absorbed in the fiber core. When referenced to the total incident solar power (100%), this corresponds to an absorption efficiency of approximately 0.02 × 26.5% = 0.53%, consistent with the value reported in the Sankey diagram and further supporting internal consistency of the model.

The model-based photon-flux analysis of the pumping cavity reveals several key limitations governing system performance. Although the cavity components work as an integrated system, losses originating in one element are compounded by imperfections in others. This interdependence complicates strict attribution of individual loss channels; however, the component-level analysis identifies several dominant limitations. First, the DM_{front}, while essential for confinement, suppress spectral bands that would otherwise contribute directly (albeit weakly) to fiber-core excitation. Second, angular dependence of reflectivity in the DM mirrors introduce cumulative confinement losses, particularly for photons undergoing multiple reflections. Thirdly, the geometry of the sensitizer layer is not optimized. Fourthly, most critically, the fiber geometry imposes a fundamental constraint. In the side-pumping configuration, the small core diameter (≈16 µm) results in a very low single-pass absorption probability, necessitating hundreds of effective core traversals for efficient excitation. Under such conditions, even minor confinement losses are magnified, placing exceptionally stringent requirements on cavity performance. Collectively, these constraints explain the limited conversion efficiency observed experimentally. The system operates near the limits imposed by photon confinement and geometric coupling, which accounts for milliwatt-level (maximum, 35 mW) laser output under 65–70 W of incident solar power.

4 | Digital Twin–Enabled Study of Design Parameter Effects on SPFL Performance

Building on the component-level analysis, a structured parametric study of the baseline configuration is now conducted. The objective is to identify which parameters fundamentally constrain performance and which offer improvement potential within the existing architectural framework, while keeping the intrinsic fiber properties fixed. Altering core parameters such as doping concentration or emission/absorption cross sections would fundamentally modify the gain dynamics and lasing behavior.

4.1 | Reflective Boundary Conditions

The primary function of the DM_{rear} is to maintain photon confinement via high reflectivity within the emission band of the sensitizer. To assess its impact on absorption efficiency, two substitutions were evaluated within the validated model. First, the DM_{rear} was replaced with a commercially available enhanced silver mirror (Thorlabs, model) providing broadband reflectivity of approximately 98%, assumed independent of wavelength and angle of incidence. Under this substitution, the fiber-core absorption efficiency decreased by nearly 10% relative to the baseline configuration. Although an ideal reflector with unity reflectance would increase absorption efficiency beyond the current 0.54%, such performance is physically unrealistic and therefore not considered further. Secondly, the DM_{rear} was then replaced by a diffuse reflector with >99% reflectance (LabSphere Spectralon). Again, a similar reduction (from 0.54% to 0.48%) in absorption efficiency was observed. Despite its high reflectivity (99.3% at ~580 nm), diffuse reflection disrupts directional confinement and increases escape probability over multiple reflections. These results indicate that the spectral and angular selectivity of the original DM_{rear} coating plays a non-trivial role in maintaining effective confinement. Simple substitution with broadband or diffuse reflectors does not improve performance within the current architecture.

4.2 | LSC Optical Guidance and Refractive Index Contrast

The simulation model follows the experimental configuration, which employs a so-called thin-film LSC as shown in Figure 1—since the thickness of the sensitizer layer is much thinner than that of the quartz substrate (80 µm << 1 mm)—rather than relying on a monolithic or bulk LSC, whereby the entire waveguide would be doped with the sensitizer. The fiber bundle is positioned within a radial region of the cylindrical cavity (3-4 cm width, approximately 75% of the radial distance from the center), allowing interaction with photons redirected within the structure. In this arrangement, the DM_{front}–DM_{rear} confinement system contributes to redirecting photons that would otherwise escape, thereby increasing the probability of interaction with the fiber region. The effectiveness of the LSC assembly depends on the refractive indices of the constituent materials (n_s—sensitizer, n_q—quartz and n_o—optical adhesive) and the resulting total internal reflection (TIR) conditions. As mentioned already, in the validated model $n_s = 1.47$ is used for sensitizer layer [19]. Manufacturer-based values were adopted for the optical adhesive ($n_o = 1.484$) [20, 25], while for the quartz glass the wavelength-dependent values were calculated according to the dispersion relation ($n_q = 1.4587$ at 580 nm) [28].

To evaluate sensitivity to refractive-index contrast, controlled perturbations were introduced around these nominal values. The resulting impact on photon confinement and fiber-core absorption efficiency was quantified. Figure 5a presents the calculated absorption efficiency as a function of n_s and n_o (step size 0.02).

The absorption-efficiency map in Figure 5a reveals a clear dependence of fiber-core absorption efficiency on refractive-index contrast within the LSC assembly. In particular, higher absorption efficiency is obtained when the refractive index of the optical adhesive approaches that of quartz ($n_q = 1.4587$ at 580 nm), minimizing refractive-index mismatch and associated interface losses. In addition, this condition improves optical coupling to the fiber, as the fibers are embedded within the adhesive and their cladding is also silica, further reducing refractive-index discontinuities in the region where photon–fiber interaction occurs. As the adhesive refractive index deviates from that of quartz, the absorption efficiency decreases, largely independent of the sensitizer refractive index.

A distinct optimum is observed at when $n_s \approx 1.43$ is minimum and $n_o \approx 1.46$, which is close to the refractive index of quartz at 580 nm pumping wavelength. This behavior can be explained by the conditions for total internal reflection. When the sensitizer refractive index is lower than that of quartz, photons are preferentially confined within the higher-index quartz layer, enhancing optical guidance toward the fiber. In contrast, when the sensitizer refractive index approaches or exceeds that of quartz, confinement is weakened, and photons are more likely to propagate into the sensitizer layer, increasing PLQY losses and reabsorption events, hence reducing the probability of interaction with the fiber core.

Consequently, optimal performance is achieved when the sensitizer refractive index is sufficiently lower than that of quartz to support TIR-based confinement, while the adhesive refractive index is closely matched to quartz to minimize interfacial losses. This explains the observed maximum in absorption efficiency within the explored parameter range, as well as the degradation in performance at higher sensitizer refractive indices (e.g., $n_s \geq 1.50$) combined with adhesive indices that deviate from quartz. These results highlight how even small changes to the optical design of the LSC assembly—in this case minimizing the refractive index contrast—offers improvement potential.

Another parameter influencing the effectiveness of the LSC structure is the thickness of the sensitizer layer. Increasing the layer thickness enhances single-pass solar absorption; however, given a PLQY of approximately 90±3% and a large (30 cm diameter) cylindrical geometry, thicker layers also amplify reabsorption losses and escape-cone losses. To evaluate this trade-off within the validated model, the sensitizer thickness was varied from 10 to

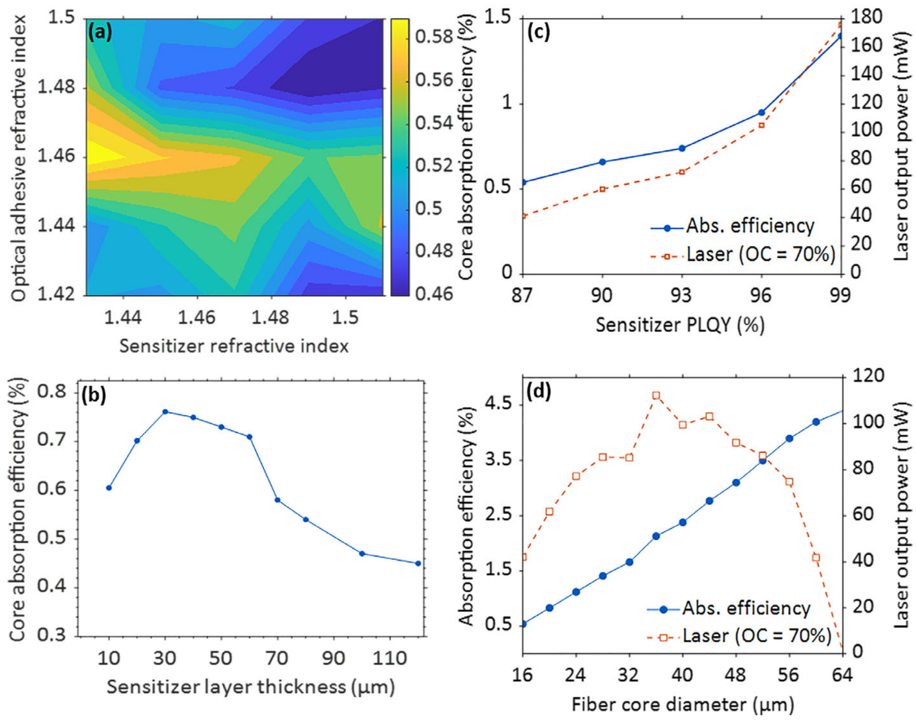

FIGURE 5 | Parameter study of SPFL performance. (a) Sensitivity of fiber-core absorption efficiency to refractive-index contrast between the sensitizer layer n_s and the optical adhesive n_o used in the LSC assembly. (b) Dependence of fiber-core absorption efficiency on sensitizer-layer thickness. (c) Influence of sensitizer PLQY on fiber-core absorption efficiency and SPFL performance. (d) Fiber-core absorption efficiency (left axis) and predicted laser output power (right axis) as a function of the core diameter, with the OC transmission fixed at 70%.

120 µm while keeping all other cavity parameters fixed (the experimental value being 80 µm). The absorption and emission spectra of the sensitizer were kept fixed, with a constant absorption coefficient corresponding to a fixed dye concentration. The optical density of the layer increases with thickness. The resulting fiber-core absorption efficiency is shown in Figure 5b. As observed, increasing the thickness beyond 80 µm leads to a reduction in absorption efficiency, whereas reducing the thickness yields an improvement. An optimal thickness of approximately 30 µm is identified within the explored range, for which the model predicts an absorption efficiency of 0.76%, corresponding to an improvement of about 40% relative to the validated baseline value of 0.54%.

For thinner layers (10–20 µm), the performance decreases, reaching 0.6%–0.7%, due to insufficient single-pass absorption of incident solar radiation. In this regime, a significant fraction of photons is not absorbed within the sensitizer layer and therefore remains susceptible to escape through the DM_{front} and DM_{rear} channels before contributing to photon recycling and fiber-core excitation. To elucidate the underlying mechanisms, a Sankey-type analysis was performed comparing the 30 and 80 µm cases, using Monte Carlo simulations with 3×10^5 photon histories. The results showed that the thinner sensitizer layer leads to increased losses through the DM_{front} and DM_{rear} channels, as a larger fraction of photons remains unabsorbed, rising by approximately 45% and 40%, respectively. However, this is offset by a substantial reduction in PLQY-related losses, which decrease from 9.1% in the 80 µm case to 4.5% in the 30 µm case, representing the dominant factor contributing to the enhanced absorption efficiency.

4.3 | Influence of Sensitizer PLQY on SPFL Performance

The Sankey analysis identified three principal material-related loss channels within the SPFL system: spectral mismatch, non-unity PLQY, and Stokes shift losses. Among these, spectral mismatch represents a more fundamental limitation associated with the electronic structure of the sensitizer and lasing materials, where substantial improvement would generally require exploration of alternative sensitizers, such as different dyes or quantum dots [33]. In contrast to fundamental spectral mismatch and Stokes shift limitations, the PLQY of the sensitizer represents a parameter that can, in principle, be improved through material engineering and optimization. This section investigates how fiber-core absorption efficiency and laser output scale with sensitizer PLQY. The analysis aims to isolate the effect of PLQY alone. Therefore, only the sensitizer PLQY was varied, from 87% to 99%, while all other optical, geometrical, and laser parameters were kept identical to the validated baseline configuration. The model predictions are presented in Figure 5c. Increasing the sensitizer PLQY from 87% to 99% resulted in a substantial enhancement of SPFL performance. For the 16 µm core-diameter fiber, the core absorption efficiency increased from 0.54% to 1.4%, while the corresponding laser output power increased to approximately 176 mW.

4.4 | Physical Size of Fiber Core

Increasing the fiber length within the DM_{front}–PTFE–DM_{rear} confinement region increases the probability of photon–core interaction and thus raises absorption efficiency, approximately linearly, as reported in [19–22]. Since the single-pass absorption probability remains governed by the small core diameter, length extension provides gains at the cost of increased configurational complexity and material usage. Moreover, extending the fiber length increases background loss in the lasing process, which can offset gains in pump absorption. Thus, fiber-length scaling introduces practical trade-offs. Given that this effect has been studied, further length scaling is not examined here.

An advantage of the developed model, which explicitly resolves the fiber geometry, is that it enables direct evaluation of the influence of fiber core size on absorption efficiency. In this study, the core diameter was treated as a secondary geometric parameter and varied from 16 to 64 μm. All other pumping and cavity parameters were kept constant, including the sensitizer layer thickness (80 μm), Nd^{3+} ion doping concentration, the outer cladding diameter (125 μm), and fiber length (400 m). As a consequence, increasing the core diameter leads to a proportional increase in the total number of Nd^{3+} ions in the system due to the enlarged active volume, while the local Nd^{3+} dopant density and core material composition are assumed unchanged. Such a parameter variation corresponds to fibers fabricated with different core diameters but the same Nd^{3+} dopant concentration.

The results presented in Figure 5d indicate that as the core diameter increases, the absorption efficiency rises approximately linearly, from 0.54% at 16 μm to 4.5% at 64 μm, corresponding to nearly an eight-fold increase. In contrast, the laser output exhibits a non-monotonic dependence on core diameter. The output power increases from 42 mW (baseline model value at 16 μm, compared to ∼35 mW experimentally) to a maximum of approximately 112 mW at a core diameter of 36 μm. Beyond this point, further increases in core diameter led to a rapid decline in laser output, reaching only 1 mW at 64 μm, despite the continued increase in absorption efficiency. This behavior can be understood by considering that, while a larger core enhances the total absorbed pump power, it also increases the effective mode area over which the pump is distributed, thereby reducing the pump intensity within the active region. As a consequence, the achievable population inversion decreases, limiting the small-signal gain despite the higher total absorbed power. The observed trend therefore indicates the presence of an optimal core diameter for a given cavity configuration, determined by the balance between maximizing absorbed pump power and maintaining sufficient inversion density for efficient gain generation. It should be noted that this behavior is obtained for an OC transmission of 70% and a sensitizer thickness of 80 μm. The identified optimal core diameter of 36 μm is therefore specific to this cavity configuration.

5 | Combined Parameter Study of SPFL Performance Using a Digital Twin

In Sections 4.1–4.4, the developed digital twin was used to investigate how individual system parameters influence fiber-core absorption efficiency and SPFL performance separately. These studies demonstrated that several parameters offer measurable performance improvements, including informed choosing refractive-indices, optimization of sensitizer-layer thickness, increased fiber-core diameter, and enhanced sensitizer PLQY. A natural question therefore arises: can these improvements be combined to achieve globally optimized SPFL performance? Addressing this question comprehensively is considerably more complex. As demonstrated throughout Sections 4.1–4.4, the performance of the present SPFL configuration (DM_{front}+LSC+DM_{rear}, surrounded by PTFE reflectors) is governed by a strongly coupled multidimensional parameter space. The key parameters include: (i) sensitizer-layer thickness, (ii) sensitizer PLQY, (iii) fiber length, (iv) fiber-core diameter, (v) refractive-index contrast within the LSC assembly, and (vi) laser-resonator output coupling (OC). A rigorous global optimization over this parameter space would require extensive coupled Monte Carlo ray-tracing and laser-model calculations across a large number of parameter combinations, which is beyond the scope of the present study Instead, the objective of this section is to investigate physically motivated combinations of selected improvement strategies in order to estimate the performance levels that may be achievable within the current SPFL architecture.

Section 4.3 demonstrated that the optimal thickness is governed by a trade-off between efficient solar-photon capture and increased losses associated with repeated reabsorption–reemission cycles under non-unity PLQY conditions. In the baseline configuration, these competing effects resulted in an optimum thickness of approximately 30 μm for the 16 μm-fiber core system. However, because the present study (of this section) assumes a substantially higher sensitizer PLQY of 99%, the losses associated with repeated reabsorption–reemission cycling are expected to be reduced. Consequently, the thickness maximizing fiber-core absorption efficiency is expected to shift. Therefore, rather than directly adopting the previously identified optimum, the sensitizer thickness was re-optimized specifically for the 36 μm-core fiber configuration under the revised 99% PLQY conditions. The corresponding dependence is shown in Figure 6a. Under these conditions, the maximum predicted fiber-core absorption efficiency reached approximately 3.85%. Interestingly, unlike the baseline 16 μm-core system—where a distinct optimum occurred near 30 μm—the high-PLQY 36 μm-core configuration exhibited a broad performance plateau. The absorption efficiency increased with sensitizer thickness up to approximately 60 μm, after which it saturated and remained nearly constant at ≈3.85% for thicknesses up to 100 μm. This behavior indicates that, under the modified conditions, increasing sensitizer thickness beyond approximately 60 μm no longer provides substantial improvement in fiber-core absorption efficiency.

Before evaluating the corresponding laser-output characteristics, a Rigrod analysis was conducted to identify the output-coupler transmission maximizing laser extraction efficiency for this configuration. Using the developed laser model, the OC reflectivity was varied from 5% to 95% in 5% increments, while the opposite cavity end was assumed to be a perfect high reflector (HR = 100%) and the fiber length was fixed at 400 m. The calculation revealed an output coupler with approximately 85% transmission as the optimal configuration. Using this optimized resonator condition together with the previously obtained absorption efficiency (3.85%), the corresponding laser-output characteristics were calculated and are presented in Figure 6b using the lasing parameters summarized in Table 1. The results indicate that, for the 36 μm-core fiber with a sensitizer PLQY of

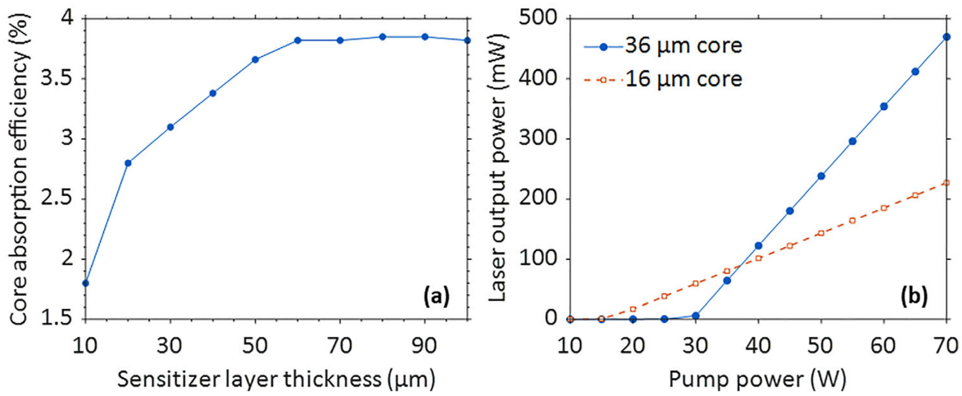

FIGURE 6 | Combined parameter study of SPFL performance. (a) Dependence of fiber-core absorption efficiency on sensitizer-layer thickness for the combined improved SPFL configuration employing a 36 μm-core fiber and sensitizer PLQY of 99%. (b) Laser-output characteristics for high-PLQY SPFL configurations employing 16 and 36 μm fiber-core diameters.

99% within the DM_{front}+LSC+DM_{rear} architecture, the optimized configuration predicts a maximum laser output power of approximately 470 mW. The corresponding lasing threshold reaching approximately 30 W. Figure 6b also includes the laser-output characteristics for the high-PLQY 16 μm-core SPFL configuration. In this case, the optimized configuration yields a lower maximum output power of approximately 227 mW—still more than a six-fold increase relative to the experimentally observed 35 mW output—but with a significantly reduced lasing threshold of approximately 15 W.

6 | Discussion

The results obtained throughout this study indicate that the performance of planar SPFLs is governed by the coupled interplay between photon confinement, sensitizer-mediated spectral conversion, and the intrinsically low probability of photon interaction with the fiber core.

Photon-flux analysis of the pumping cavity revealed two broad categories of losses within the DM_{front} + LSC + DM_{rear} architecture. The first corresponds to material-related losses (≈51.2%), including spectral mismatch, non-unity PLQY, and Stokes-shift losses. These losses are fundamentally linked to the optical and electronic properties of the sensitizer and lasing medium and can therefore only be substantially improved through advances in material engineering, such as development of sensitizers with improved spectral matching and higher PLQY. The second category corresponds to cavity-related confinement losses (≈48.3%), which remain comparably large despite the use of DM-facilitated photon-confinement architecture.

The origin of these confinement losses can be traced to the extremely low probability of photon interaction with the fiber core. Owing to the micrometer-scale core diameter and relatively small absorption cross section of the active Nd^{3+}-doped fiber core, efficient excitation requires photons to undergo a large number of recirculation events within the cavity before absorption occurs. Under these conditions, even relatively small confinement imperfections become strongly amplified. The model showed that approximately 82.8% of cavity photons never interacted with the fiber core at all, directly illustrating the severity of the photon-coupling limitation.

Although incorporation of the LSC sensitizer layer substantially enhances photon harvesting and has enabled current state-of-the-art experimental demonstrations of planar SPFLs, it simultaneously introduces additional constraints. In particular, the results revealed that sensitizer PLQY and repeated reabsorption–reemission processes strongly influence overall system performance. Increasing the sensitizer PLQY from 87% to 99% improved the absorption efficiency of the 16 μm-core configuration from 0.54% to 1.4%, identifying material quality as one of the key factors governing achievable efficiency. Furthermore, because photon guidance within the LSC critically depends on total internal reflection, the refractive-index distribution of the sensitizer–adhesive–quartz assembly becomes an important design parameter. The geometry of the sensitizer layer also plays a major role, with the simulations demonstrating strong sensitivity of SPFL performance to sensitizer thickness.

Combining several physically motivated improvement strategies within the present architecture resulted in a predicted maximum laser output power of approximately 470 mW, corresponding to a ≈13-fold improvement relative to the experimentally demonstrated maximum laser output reported in [22]. The corresponding solar-to-laser conversion efficiency remains limited to ≈0.7%. These results indicate that, despite significant improvement potential, planar one-sun SPFLs remain fundamentally constrained by photon-confinement and photon–core interaction limitations.

The achieved fiber-core absorption efficiency of 3.85% (corresponding to ≈2.7 W of absorbed power in a 400 m fiber with a 36 μm core diameter) provides important context for assessing the effectiveness of the LSC-assisted pumping strategy. Although this represents a substantial improvement over the experimentally validated baseline case, it remains low compared with the spectrally accessible fraction of incident solar power. According to the Sankey analysis, approximately 60% of the incident AM1.5G solar power is spectrally usable within the present architecture, whereas only 3.85% of the total incident solar power was ultimately absorbed within the fiber core under the best-performing simulated configuration. From this perspective, substantial further improvements are still required in both material-related losses and cavity-confinement efficiency. In particular, future SPFL architectures must achieve more efficient coupling of solar and sensitized photons into the fiber core in order to approach the solar-to-laser efficiencies already demonstrated in concentrated solid-state SPLs [6, 34] and the double-digit efficiency target [8].

The sensitivity of the model to selected physical and geometrical parameters is examined in Figure 5, while the convergence analysis in Figure 2a confirms that Monte Carlo statistical fluctuations are small at the adopted photon counts. Together with the agreement between the predicted and measured differential gain and laser-output characteristics, these results support the robustness of the main conclusions within the investigated parameter ranges.

7 | Conclusions

One-sun solar-pumped planar LSC-assisted fiber lasers were investigated using a Monte Carlo ray-tracing model with explicit geometric representation of the fiber coils and fiber core, combined with a coupled rate-equation and power-propagation framework. The model was validated against experimentally measured differential gain and laser output characteristics, demonstrating good agreement and establishing a consistent physics-based digital twin of the SPFL system.

The analysis showed that system performance is fundamentally limited by inefficient photon–core interaction. The micrometer-scale fiber-core diameter together with the relatively small absorption cross section of the Nd^{3+}-doped gain medium results in a very low single-pass absorption probability ($\sim 10^{-3}$), requiring photons to undergo a large number of recirculation events before absorption occurs. Under these conditions, even moderate optical losses within the cavity accumulate and significantly reduce effective pump utilization.

Component-level analysis revealed that spectral filtering at the dichroic mirrors, incomplete absorption and reabsorption within the sensitizer layer, finite sensitizer PLQY, and angular-dependent mirror reflectivity collectively determine the overall confinement efficiency. The results indicate that planar one-sun SPFLs are not limited by a single dominant loss mechanism, but rather by the coupled interaction between weak photon–core coupling and imperfect photon confinement.

The digital twin–enabled parameter studies further demonstrated how SPFL performance is influenced by the refractive-index distribution of the LSC assembly, sensitizer PLQY, sensitizer-layer geometry, and fiber-core diameter. Combining several physically motivated improvement strategies within the present architecture resulted in a predicted maximum laser output power of approximately 470 mW for a 400 m fiber with a 36 μm core diameter and sensitizer PLQY of 99%, corresponding to an approximately 13-fold improvement relative to the experimentally demonstrated maximum output reported in [22]. In addition, the simulations predicted that, for a 16 μm-core fiber with sensitizer PLQY of 99%, the lasing threshold could be reduced to approximately 15 W.

The validated digital twin developed in this work provides a systematic framework for investigating alternative SPFL architectures, cavity configurations, and parameter combinations, enabling physics-guided exploration and optimization of future one-sun SPFL systems.

Author Contributions

Anvarjon Sherniyozov: conceptualization, methodology, software, data curation, investigation, validation, formal analysis, visualization, writing – original draft. **Dmitry Busko**: methodology, validation, investigation. **Bryce S. Richards**: conceptualization, funding acquisition, writing – review and editing, visualization, methodology, supervision, resources, project administration, formal analysis.

Acknowledgements

The authors gratefully acknowledge financial support received from: i) the Helmholtz Association Research Field Energy: Program Materials and Technologies for the Energy Transition (Topic 1 Photovoltaics and Wind Energy, ref. 38.01.05); ii) the European Union's Horizon Europe Research and Innovation Programme under Grant Agreement No. 101161312 (European Innovation Council (EIC) Pathfinder Challenge project APACE). Finally, Prof. Masamori Endo from Tokai Univ. (Japan) is gratefully acknowledged for providing SPFL experimental parameters.

Conflicts of Interest

The authors declare no conflicts of interest.

Data Availability Statement

The data that support the findings of this study are available from the corresponding author upon reasonable request.

References

1. T. Yabe, T. Ohkubo, D. T. Hung, H. Kuboyama, J. Nakano, and K. Okamoto, "Demonstration of Solar-Pumped Laser-Induced Magnesium Production From Magnesium Oxide," *Magnesium Technology*, eds. S. N. Mathaudhu, W. H. Sillekens, N. R. Neelameggham, and N. Hort, (Springer, 2012), 55–58, https://doi.org/10.1007/978-3-319-48203-3_10.

2. M. Küblböck, J. Will, and H. Fattahi, "Solar Lasers: Why not?," *APL Photonics* 9 (2024): 050903, https://doi.org/10.1063/5.0209355.

3. D. A. Lamarre, G. R. Simpson, and M. R. Thorburn, "Sun-Powered Lasers," *Journal of the Franklin Institute* 274 (1962): 531–532, https://doi.org/10.1016/0016-0032(62)90065-0.

4. Z. J. Kiss, H. R. Lewis, and R. C. Duncan Jr., "Sun Pumped Continuous Optical Maser," *Applied Physics Letters* 2 (1963): 93–94, https://doi.org/10.1063/1.1753794.

5. C. G. Young, "A Sun-Pumped CW One-Watt Laser," *Applied Optics* 5 (1966): 993–997, https://doi.org/10.1364/AO.5.000993.

6. D. Liang, C. R. Vistas, D. Garcia, et al., "Most Efficient Simultaneous Solar Laser Emissions From Three Ce:Nd:YAG Rods Within A Single Pump Cavity," *Solar Energy Materials and Solar Cells* 246 (2022): 111921, https://doi.org/10.1016/j.solmat.2022.111921.

7. S. Payziyev, A. Sherniyozov, S. Bakhramov, et al., "Luminescence Sensitization Properties of Ce:Nd:YAG Materials for Solar Pumped Lasers," *Optics Communications* 499 (2021): 127283, https://doi.org/10.1016/j.optcom.2021.127283.

8. D. Graham-Rowe, “Solar-Powered Lasers,” *Nature Photonics* 4 (2010): 64–65, https://doi.org/10.1038/nphoton.2009.272.

9. P. Guo, J. Zhang, Z. Chen, et al., “Side-Pumped Solar Nd-Doped Fiber Laser Based on Off-Axis Parabolic Mirror Array,” *Optik* 271 (2022): 170096, https://doi.org/10.1016/j.ijleo.2022.170096.

10. S. Payziyev, A. Sherniyozov, and A. Qakhkhorov, “Simulation of Solar-Pumped Multicore Nd^{3+}-Doped Silica Fiber Lasers,” *Journal of Photonics for Energy* 14 (2024): 024502, https://doi.org/10.1117/1.JPE.14.024502.

11. D. Garcia, “Primary Solar Concentrators,” *Solar-Pumped Lasers*, eds. D. Liang, J. Almeida, C. Vistas, B. Tibúrcio, and D. Garcia, (Springer Nature, 2023), https://doi.org/10.1007/978-3-031-24785-9_5.

12. T. Masuda, M. Iyoda, Y. Yasumatsu, et al., “A Fully Planar Solar Pumped Laser Based on a Luminescent Solar Collector,” *Communications Physics* 3 (2020): 60, https://doi.org/10.1038/s42005-020-0326-2.

13. M. Endo and J.-F. Bisson, “Positive Gain Observation in a Nd-Doped Active Fiber Pumped by Low-Concentrated Solar-Like Xenon Lamp,” *Japanese Journal of Applied Physics* 51 (2012): 022701, https://doi.org/10.1143/JJAP.51.022701.

14. T. Masuda, M. Iyoda, Y. Yasumatsu, and M. Endo, “Low-Concentrated Solar-Pumped Laser via Transverse Excitation Fiber-Laser Geometry,” *Optics Letters* 42 (2017): 3427–3430, https://doi.org/10.1364/OL.42.003427.

15. J.-F. Bisson, M. Iyoda, Y. Yasumatsu, M. Endo, and T. Masuda, “Effect of the Thermally Excited Lower Laser Level in a Neodymium-Doped Fiber,” *Journal of the Optical Society of America B* 36 (2019): 736–745, https://doi.org/10.1364/JOSAB.36.000736.

16. M. Endo, J.-F. Bisson, and T. Masuda, “Monte Carlo Simulation of a Transversely Excited Solar-Pumped Fiber Laser,” *Japanese Journal of Applied Physics* 58 (2019): 112006, https://doi.org/10.7567/1347-4065/ab4a93.

17. J. Marques-Hueso, R. Peretti, R. Abargues, B. S. Richards, C. Seassal, and J. P. Martínez-Pastor, “Photonic Crystal-Driven Spectral Concentration for Upconversion Photovoltaics,” *Advanced Optical Materials* 3 (2015): 568–574, https://doi.org/10.1002/adom.201400402.

18. T. Masuda, Y. Zhang, C. Ding, et al., “All-Inorganic Cesium Lead Halide Perovskite Nanocrystals for Solar-Pumped Laser Application,” *Journal of Applied Physics* 127 (2020): 243104, https://doi.org/10.1063/5.0011945.

19. S. Dottermusch, T. Masuda, M. Endo, B. S. Richards, and I. A. Howard, “Solar Pumping of Fiber Lasers With Solid-State Luminescent Concentrators: Design Optimization by Ray Tracing (Advanced Optical Materials 12/2021),” *Advanced Optical Materials* 9 (2021): 2170043, https://doi.org/10.1002/adom.202170043.

20. T. Masuda, K. Aoyagi, S. Dottermusch, I. A. Howard, B. S. Richards, and M. Endo, “Light Management for Enhancing Optical Gain in a Solar-Pumped Fiber Laser Employing a Solid-State Luminescent Solar Concentrator,” *Advanced Photonics Research* 3 (2022): 2100214, https://doi.org/10.1002/adpr.202100214.

21. M. Endo, K. Yamamoto, S. Dottermusch, et al., “Solar-Pumped Fiber Laser Using a Solid-State Luminescent Solar Collector,” *Optics Express* 31 (2023): 26040–26053, https://doi.org/10.1364/OE.496268.

22. M. Endo, R. Tomizawa, T. Nagano, and K. Hayashi, “Fully Planar Solar-Pumped Fiber Laser With 0.1% Slope Efficiency,” *Optics Letters* 49 (2024): 5831–5833, https://doi.org/10.1364/OL.531496.

23. M. Endo, R. Tomizawa, T. Nagano, and K. Hayashi, “Fully Planar Solar-Pumped Fiber Laser With 0.1% Slope Efficiency,” *Optics Letters* 49 (2024): S5831–S5833, https://doi.org/10.6084/m9.figshare.27004411.

24. M. Endo, R. Tomizawa, T. Nagano, K. Hayashi, and Q. Shen, “Computational Analysis of the Efficiency Limit of a Fully Planar Solar-Pumped Laser,” *Applied Optics* 64 (2025): S9769–S9775, https://doi.org/10.6084/m9.figshare.30374986.

25. Norland Products Inc. *Norland Optical Adhesive 85 (NOA 85) Technical Data Sheet* (Norland Products Inc., 2025), https://norlandproducts.com/wp-content/uploads/2025/03/NOA-85-TDS.pdf.

26. A. E. Siegman, *Lasers* (University Science Books, 1986).

27. C. R. Giles and E. Desurvire, “Modeling Erbium-Doped Fiber Amplifiers,” *Journal of Lightwave Technology* 9 (1991): 271–283, https://doi.org/10.1109/50.65886.

28. I. H. Malitson, “Interspecimen Comparison of the Refractive Index of Fused Silica*,†,” *Journal of the Optical Society of America* 55 (1965): 1205–1209, https://doi.org/10.1364/JOSA.55.001205.

29. D. Gloge, “Weakly Guiding Fibers,” *Applied Optics* 10 (1971): 2252–2258, https://doi.org/10.1364/AO.10.002252.

30. M. M. Mann and L. G. DeShazer, “Energy Levels and Spectral Broadening of Neodymium Ions in Laser Glass,” *Journal of Applied Physics* 41 (1970): 2951–2957, https://doi.org/10.1063/1.1659342.

31. T. Masuda, M. Iyoda, Y. Yasumatsu, and M. Endo, “Low-Loss Pigtail Reflector for Fiber Lasers,” *Review of Scientific Instruments* 88 (2017): 053112, https://doi.org/10.1063/1.4983924.

32. J. A. Caird, A. J. Ramponi, and P. R. Staver, “Quantum Efficiency and Excited-State Relaxation Dynamics in Neodymium-Doped Phosphate Laser Glasses,” *Journal of the Optical Society of America B* 8 (1991): 1391–1403, https://doi.org/10.1364/JOSAB.8.001391.

33. M. Endo, R. Tomizawa, T. Nagano, K. Hayashi, and Q. Shen, “Computational Analysis of the Efficiency Limit of a Fully Planar Solar-Pumped Laser,” *Applied Optics* 64 (2025): 9769–9775, https://doi.org/10.1364/AO.575837.

34. D. Liang, H. Costa, B. D. Tibúrcio, C. R. Vistas, and J. Almeida, “High-Efficiency Solar-Pumped Lasers,” *Advances in Physics: X* 10 (2025), 2531056, https://doi.org/10.1080/23746149.2025.2531056.